

Spatial substructure hybrid simulation tests of high-strength steel composite Y-eccentrically braced frames

Tengfei Li^{1a}, Mingzhou Su^{*1,2} and Yan Sui^{1,2}

¹School of Civil Engineering, Xi'an University of Architecture and Technology, Xi'an 710055, P.R. China

²Key Lab of Structural Engineering and Earthquake Resistance, Ministry of Education (XAUAT), Xi'an 710055, P.R. China

(Received August 17, 2019, Revised December 27, 2019, Accepted December 28, 2019)

Abstract. High-strength steel composite Y-eccentrically braced frame (Y-HSS-EBF) is a novel structural system. In this study, the spatial substructure hybrid simulation test (SHST) method is used to further study the seismic performance of Y-HSS-EBF. Firstly, based on the cyclic loading tests of two single-story single-span Y-HSS-EBF planar specimens, a finite element model in OpenSees was verified to provide a reference for the numerical substructure analysis model for the later SHST. Then, the SHST was carried out on the OpenFresco test platform. A three-story spatial Y-HSS-EBF model was taken as the prototype, the top story was taken as the experimental substructure, and the remaining two stories were taken as the numerical substructure to be simulated in OpenSees. According to the test results, the validity of the SHST was verified, and the main seismic performance indexes of the SHST model were analyzed. The results show that, the SHST based on the OpenFresco platform has good stability and accuracy, and the results of the SHST agree well with the global numerical model of the structure. Under strong seismic action, the plastic deformation of Y-HSS-EBF mainly occurs in the shear link, and the beam, beam-columns and braces can basically remain in the elastic state, which is conducive to post-earthquake repair.

Keywords: high strength steel; Y-eccentrically braced frame; link; spatial substructure; hybrid simulation

1. Introduction

In recent years, steel structures have played an increasingly important role in the construction practice because of their light weight, high strength, good plasticity and toughness, easy manufacturing and installation, short construction period, etc. According to the different layouts of structural elevation, steel structure systems can be divided into moment-resisting steel frame systems, concentrically braced steel frame systems, eccentrically braced steel frame (EBF) systems, and frame-tube structure systems. The EBF system refers to the bracing inclined bars in the structural system, which have at least one end connected with a beam (not at the column joint), whereas the other end can be connected at the intersection of the beam and the column, or at the connection point which deviates from the other brace, and forms the link between the brace and the column, or between two braces. EBFs have the advantages of both concentrically braced structures and moment-resisting frame structures. They can provide enough elastic stiffness to meet the requirements of story drifts under frequent earthquakes. Under seldom

earthquakes, seismic energy is dissipated by plastic deformation of the link, while other structural components remain in the elastic stage (Ricles and Popov 1994). Fig. 1 shows the typical layout of an EBF. The e represents the length of the link in the EBF. When $e \leq 1.6M_p/V_p$, the link belongs to the shear yielding type, where M_p and V_p are the plastic bending capacity and plastic shear capacity of link, respectively. When e is in the range from $1.6M_p/V_p$ to $2.6M_p/V_p$, the link is of the bending-shear yielding type (Kasai and Popov 1986). According to the suggestions of GB 50011-2010, the link of an EBF should be designed as the shear yield type, because the internal force of the shear link is controlled by the shear force, whereas the plastic deformation develops sufficiently and the energy dissipation capacity is excellent.

Y-EBF (Fig. 1(a)) is one of the structural forms of EBFs. Although its lateral stiffness is slightly lower compared with other bracing forms, the section size and length of the link can be designed separately to optimize the performance of the whole structure, because its link is located outside the frame beam. Moreover, under strong seismic action, plastic deformation mainly concentrates in the link section, while the least damage is sustained by frame beams and floor slabs, so they are easy to repair after an earthquake (Mansour *et al.* 2011, Shayanfar *et al.* 2012). In order to take full advantage of the plastic deformation of the link, the internal forces of the non-energy-dissipating members are amplified by the GB 50011-2010, which often causes the section of the member to be too large and limits the application of this structural form. In recent years, the strength and processing properties of steel have been greatly

*Corresponding author, Professor
E-mail: sumingzhou@xauat.edu.cn

^a Ph.D. Student
E-mail: litengfei0217@163.com

^b Ph.D.
E-mail: suiyanmyy@163.com

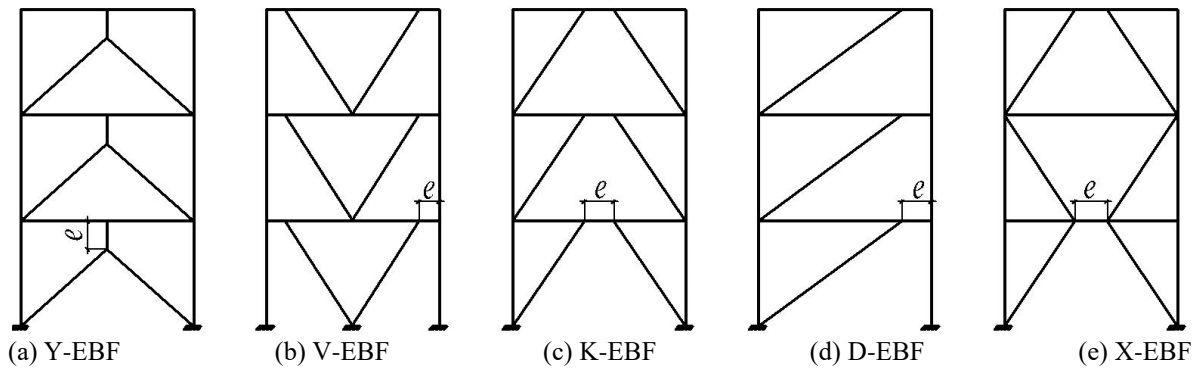


Fig. 1 The typical layout of EBF

improved by new steel production. Researchers began to study the mechanical properties of high-strength steel (usually steel with nominal yield strength of 460 MPa or above) (Alhendi and Celikog 2015, Chiew *et al.* 2015, Kim *et al.* 2014, Shi *et al.* 2012). The use of high-strength steel can effectively reduce the cross-section of frame beams and columns. However, when the strength of high-strength steel increases the yield ratio inevitably increases and elongation deteriorates. It is difficult to meet the requirements of the steel yield ratio and elongation in GB 50011-2010, which also limits the application of high-strength steel in seismic fortification areas (Ban and Shi 2017). In order to solve this problem, the high-strength steel composite Y-eccentrically braced frames (Y-HSS-EBFs) are proposed. The link is made of ordinary steel (e.g., LYP225, Q235, or Q345 steel with the nominal yield strength of 225, 235, and 345 MPa respectively) with good deformation ability, while the frame beam and column are made of high strength steel. Under seldom earthquake action, the link enters the plastic state completely in order to dissipate energy, so as to ensure that the structure has good plastic deformation and energy dissipation capacity, while the frame beam and frame column are still in the elastic state or developing slight plasticity, so high-strength steel can be used to save material and reduce cost.

Although some scholars have carried out theoretical analyses and experimental research on this structural form (Popov 1983, Shayanfar *et al.* 2011, Montuori *et al.* 2014a, b), the research on Y-HSS-EBFs is relatively scarce at present. Duan and Su (2017) carried out monotonic and cyclic loading tests on plane Y-HSS-EBF specimens. Taking the length of the link as a variable, the failure mechanism, stiffness and hysteretic performance of specimens with shear and flexural links were studied. Wang *et al.* (2016) carried out a quasi-static test of a three-story half-scale Y-HSS-EBF. Test results reveal that Y-HSS-EBF has high stiffness and load-carrying capacity, and the shear link has good energy dissipation. Lian *et al.* (2015) compared seismic performance and economy of HSS-EBFs versus EBFs using nonlinear hysteretic and time history analyses. Results indicate that the seismic performance of HSS-EBFs is slightly lower than that of EBFs under the same design conditions. For the 12, 16, and 20-story designs, the weight decrease ratios of HSS-EBFs relative to EBFs are 16%, 12% and 7%, respectively.

In this study, a new substructure hybrid simulation test (SHST) method is used to further investigate the seismic performance of Y-HSS-EBFs. SHST combines the substructure pseudo-dynamic test (Dermitzakis and Mahin 1985) with general finite element software, taking the vulnerable part of the whole structure as the experimental substructure, and simulating the remaining part using finite elements, which can complement large-scale tests with very good prospects for practical applications (Chae *et al.* 2013, Hashemi and Mosqueda 2014, Khan *et al.* 2018). Firstly, on the basis of existing quasi-static cyclic loading tests, a finite element model in OpenSees was verified to provide a reference for the numerical substructure analysis model for the later SHST. Then, the SHST was carried out on the OpenFresco test platform. A three-story spatial Y-HSS-EBF model was taken as the prototype, the top story was taken as the experimental substructure, and the seismic performance of the structure was studied according to test results.

2. Verification of the finite element model in SHST

In SHST, the accuracy of numerical substructure modeling will have a significant impact on the validity of the test results. In this section, the OpenSees FE model is validated based on the pseudo-static test of Y-HSS-EBF by Duan and Su (2017) to provide a reference for the numerical substructure analysis model for the later SHST.

In reference Duan and Su (2017), the author's research group performed two pseudo-static cyclic loading tests of half-scale single-story single-span Y-HSS-EBF plane specimens. The links were of shear yield type with lengths of 300 mm (Specimen Y1) and 500 mm (Specimen Y2). The test model is shown in Fig. 2. The frame beams, columns and braces were made of Q460 steel, while the shear links were made of Q345 steel. The test results of material properties are shown in Table 1. The span of the specimens was 3600 mm and the story height was 1800 mm. The sections of the members were as follows: the frame column was H150×150×6×10, the frame beam was H225×125×6×10, the shear link section was H225×125×6×10, the brace section was H125×120×6×10, and all joints in the model were welded in full penetration.

As shown in Fig. 2(c), the jacks were used to exert a vertical load on top of the column, and the actuator was

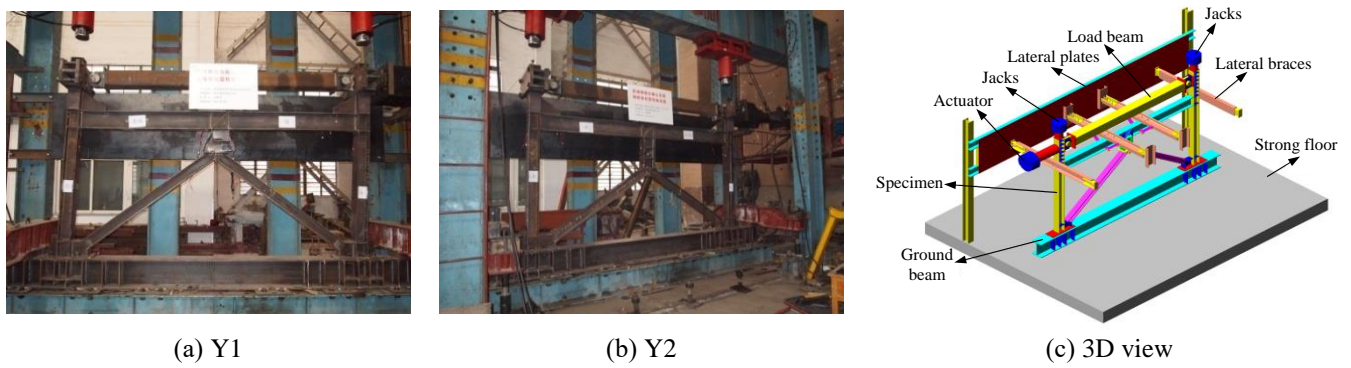


Fig. 2 Test setup in reference Duan and Su (2017)

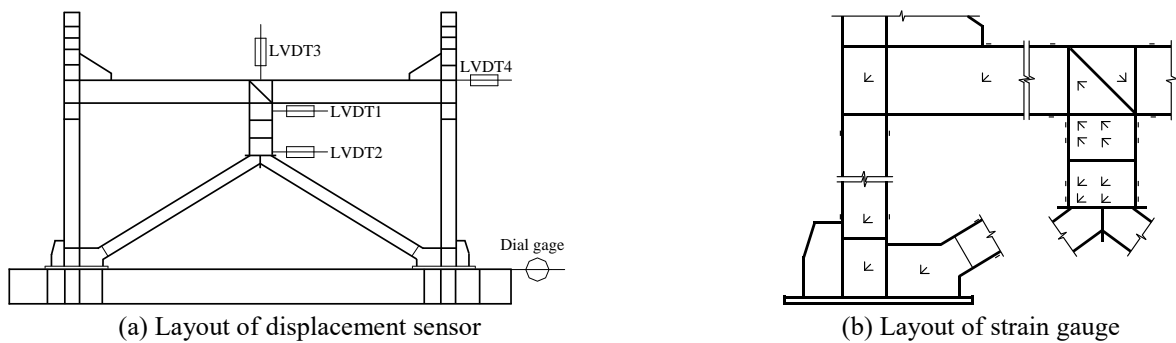


Fig. 3 Instrumentation arrangement of the specimen in reference Duan and Su (2017)

Table 1 Material properties of steel

Thickness (mm)	Yield strength f_y (MPa)	Ultimate strength f_u (MPa)	Elastic modulus E (10^5 MPa)	Elongation δ (%)
6	427.40	571.10	2.01	29.73
10	383.33	554.40	2.00	35.88
8	496.90	658.57	2.08	26.53
10	468.77	627.97	2.02	31.01

Table 2 Cyclic loading protocols

Series	Control type	Control indicators (column top)	
		Force (kN)	Displacement (mm)
1	load	$0.25P_y$ *(1 cycle)	—
2	load	$0.50P_y$ (1 cycle)	—
3	load	$0.75P_y$ (1 cycle)	—
4	load	$1.00P_y$ (1 cycle)	—
5	displacement	—	$1.0\Delta_y$ *(3 cycles)
6	displacement	—	$2.0\Delta_y$ (3 cycles)
7	displacement	—	$3.0\Delta_y$ (3 cycles)
8	displacement	—	$4.0\Delta_y$ (3 cycles)
9	displacement	—	$4.5\Delta_y$ (3 cycles)
10	displacement	—	$n \times \Delta_y$ (3 cycles)

* P_y : Evaluated yielding load of specimens; Δ_y : Evaluated yielding displacement of specimens

used to exert a horizontal load. The horizontal load was transmitted to the frame column on the other side through a pin-ended load beam. Cyclic loading protocols of mixed control of load and displacement was adopted. The specific

loading stages are shown in Table 2. Fig. 3 shows the instrumentation arrangement of measuring points. The lateral displacement of the specimens and the rotation value of the shear links were measured by the linear variable

Table 3 Parameters of Steel02

Steel	f_y (MPa)	E (10^5 MPa)	b	R_0	cR_1	cR_2	a_1	a_2	a_3	a_4
Q345B	405.365	2.00	0.01–0.02	18.5	0.925	0.1	0	1	0	1
Q460C	482.835	2.05	0.01–0.02	18.5	0.925	0.1	0	1	0	1

Table 4 The control parameters of the shear spring

Shear spring parameters	Steel02 parameters	Specific corresponding values (Y1)	Specific corresponding values (Y2)
Yield shear force of shear link V_y	Yield strength f_y	334.329 kN	325.231 kN
Shear line stiffness of shear link K_0	Elasticity modulus E	316.172 kN/mm	189.703 kN/mm

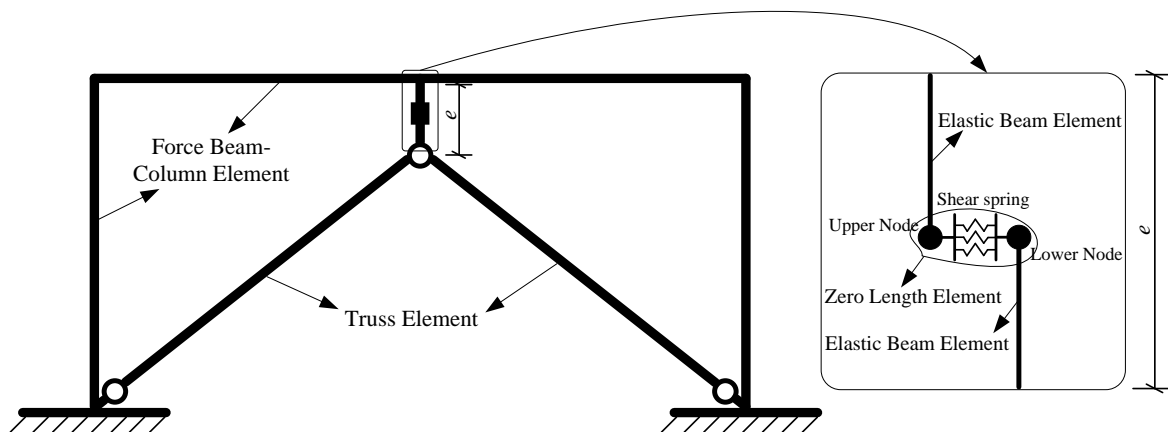


Fig. 4 Finite element model

displacement transducers (LVDTs). The strain gauges were arranged at the beam-column joint, brace, and shear link section.

2.1 Establishing the finite element model

The size of the model is the same as that of the test specimens, and the material nonlinearity and geometric nonlinearity are considered. The finite element model is shown in Fig. 4. Force Beam-Column Elements are used for the frame beam and column, and Truss elements with hinged ends are used for the brace. Steel02 (Menegotto 1973), in which isotropic strain hardening and the Bauschinger effect can be taken into account, can be used for constitutive selection of steels. The yield strength and elastic modulus E of materials are averaged according to the measured results of the material properties tests in Table 1. According to the specifications of steel strain hardening rate b in OpenSees user command-language manual (Mazzoni *et al.* 2009), the author initially selected it with the range of 0.01–0.02, and then determined the final value of b through many simulation attempts. The three shape control parameters of the curve transition sections R_0 , cR_1 , cR_2 , and the isometric reinforcement parameters a_1 – a_4 are selected by referring to the discussion of results in the OpenSees

user command-language manual (Mazzoni *et al.* 2009) on the influence of the values of the parameters. The specific values are shown in Table 3.

Establishing a reasonable shear link element model is the key problem to finite element modeling and analysis of Y-HSS-EBFs. The link in reference Duan and Su (2017) is designed as a shear yield type, and the shear force remains constant throughout the link section. Therefore, a non-linear shear hinge is set in the middle of the link by using a zero-length element, assuming that the shear deformation only occurs in the hinge, and the bending and axial deformation are borne by the elastic beam elements on both sides. In other words, the shear stiffness of link will be considered by the zero-length element, and the flexural stiffness will be considered by the elastic beam elements.

Zero-length elements need to define material properties in six directions, only considering the shear direction plastic deformation in the plane, while material properties in other directions are rigid. The key problem of modeling is to determine the restoring force parameters of the shear direction spring reasonably, which is also simulated by Steel02. In the zero-length element, the yield strength f_y of the Steel02 material corresponds to the yield shear force V_y of the shear link section, and the elastic modulus E corresponds to the shear line stiffness K_0 of the shear link.

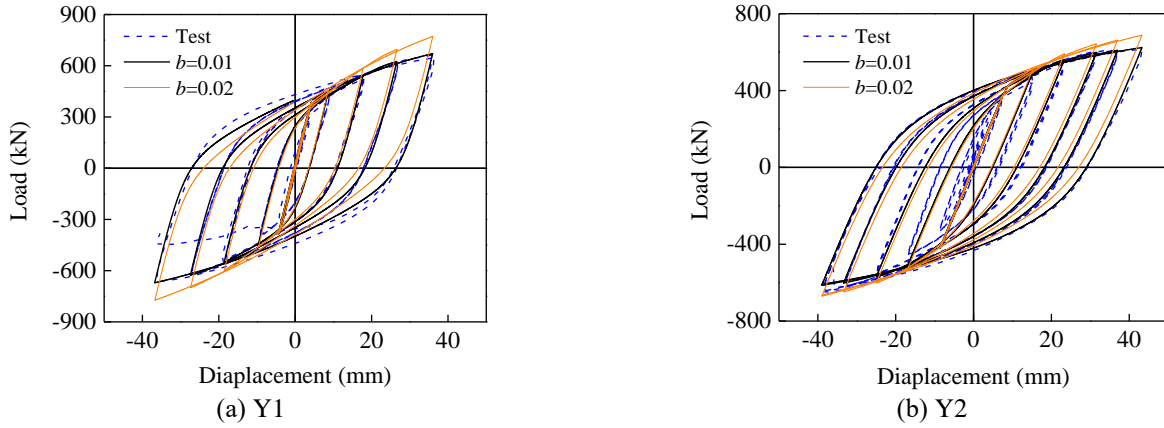


Fig. 5 Comparison of hysteretic loops

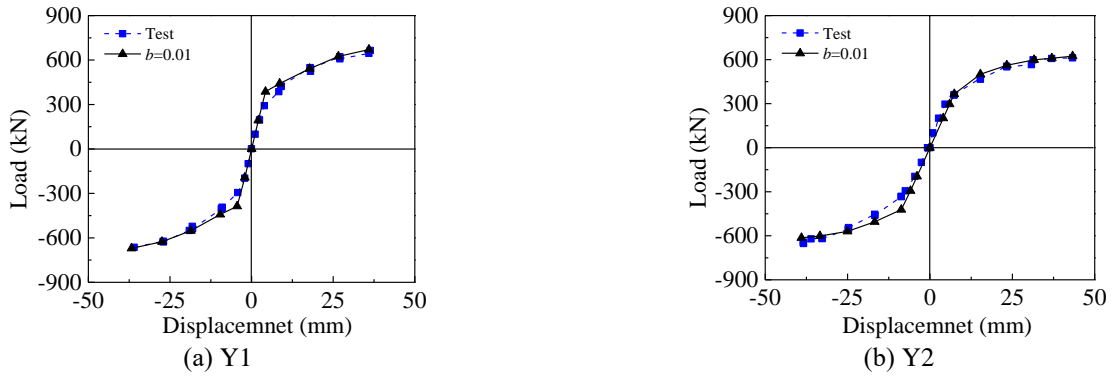


Fig. 6 Comparison of skeleton curve

The initial yield shear force calibrated in reference Özhendekci and Özhendekci (2008) can be calculated through the following equation

$$V_y = 1.1\alpha V_p \quad (1)$$

$$\alpha = 1 + \frac{A_f^2 - 0.0625(et_w)^2}{0.58A_w b_f e} \quad (2)$$

where, α is the shear capacity enhancement factor considering the flange, $V_p = 0.58 f_{y,w} A_w$, A_w and A_f are the cross-section area of shear link web and single flange, e is the length of shear link, t_w is the web thickness, b_f is the width of flange, $f_{y,w}$ is the yield strength of shear link web. The average value of Q345 steel is taken according to the coupon test in reference Duan and Su (2017).

The calculation of shear line stiffness K_0 could be calculated as

$$K_0 = GA/e = GA_w/e \quad (3)$$

where G is the shear modulus of the link section, equals to 80GPa.

According to Eqs. (1) and (3), the control parameters of two model shear springs and corresponding parameters of steel02 are obtained as shown in Table 4.

2.2 Verifying the finite element model

In order to verify the reliability of the numerical simulation, the hysteresis curves and skeleton curves of the two specimens are compared with the experimental results.

2.2.1 Comparison of hysteretic loops

As shown in Fig. 5, the experimental hysteresis loops of Y1 and Y2 are compared with the simulation ones when b is 0.01 and 0.02 respectively. It can be seen from the figure that when b is selected as 0.01, the simulation results are in better agreement with the experimental results in both loading and unloading stages. There are some differences between the test and the simulation results when the specimen Y1 is damaged. This is mainly due to the failure of the specimen Y1 due to local buckling and tearing of the web of the shear link during the test, while the initial defects of the member are not considered in the finite element method, so the bearing capacity does not suddenly decrease.

2.2.2 Comparison of skeleton curves

As shown in Fig. 6, the skeleton curves of the finite element model when b is 0.01 are compared with the experimental results. It can be seen that they are in good agreement, and the finite element skeleton curve is close to

Table 5 Comparison of the results of FEM calculation and the test values of Y1

Loading direction	Performance indicators	Lateral stiffness K_i (kN·mm ⁻¹)	Yield point		Ultimate point		Ductility μ
			Δ_y (mm)	F_y (kN)	Δ_u (mm)	F_u (kN)	
Positive direction (push)	FEM	86.25	7.78	430.00	35.96	671.00	4.62
	Test	79.62	8.35	386.66	36.34	664.86	4.35
	Error*	8.32	-6.82	11.20	-1.05	0.92	6.20
Negative direction (pull)	FEM	89.82	7.47	419.23	36.76	671	4.92
	Test	83.54	7.94	374.01	36.00	663.31	4.53
	Error*	7.52	-5.91	12.09	2.11	1.15	8.53

*Error=(Finite element-Test)/Test×100%

Table 6 Comparison of the results of FEM calculation and the test values of Y2

Loading direction	Performance indicators	Lateral stiffness K_i (kN·mm ⁻¹)	Yield point		Ultimate point		Ductility μ
			Δ_y (mm)	F_y (kN)	Δ_u (mm)	F_u (kN)	
Positive direction (push)	FEM	73.91	8.44	385.45	43.27	623.83	5.12
	Test	81.20	7.54	364.75	43.28	612.27	5.74
	Error	-8.97	11.93	5.67	-0.02	1.88	-10.68
Negative direction (pull)	FEM	65.02	9.44	421.21	39	613.84	4.13
	Test	70.75	9.10	361.96	38.44	643.89	4.22
	Error	-8.10	3.73	16.37	1.45	-4.668	-2.19

the test results in bearing capacity and lateral stiffness. Tables 5 and 6 show the comparison between results of the finite element model (FEM) calculation and test results for Y1 and Y2 in each loading stage. From Tables 5 and 6, it can be seen that the yield load obtained in FEM is slightly higher than the test results, and the ultimate load is in good agreement with the test results.

Based on the above analysis, it is clear that the finite element model in OpenSees is reliable and can be used to model the numerical substructure in the follow-up SHST.

3. SHST model

In this section, the SHST method is used to further study the seismic performance of the Y-HSS-EBF structure.

3.1 Prototype structure

The prototype structure is designed according to GB5011-2010. As shown in Fig. 7, the plane dimension of the prototype structure is 5650 mm by 5650 mm, with three stories and a height of 3600 mm. The frame beams and columns are made of Q460 steel, the links are made of Q235 steel, the braces are made of Q345 steel, and the brace form is Y-shaped. The length of the link (which is a shear yield type) is 700 mm. The cross-sectional dimensions of each member are shown in Table 7. According to GB5011-2010, the design peak ground acceleration (PGA) of the prototype structure is 0.2 g with a 10% exceeding probability in 50 years.

Table 7 Cross section of the member

Member	Cross section (mm)	
Column	H290×290×16×20	
Beam	H280×200×16×20	
Brace	H200×200×12×20	
Shear link	1 st floor	H250×140×8×16
	2 nd floor	H200×140×8×16
	3 rd floor	H160×140×6×16

3.2 The SHST model

Considering the conditions of the laboratory, a half-scale model of the prototype structure was selected for the SHST model. The height of the model is 1800 mm, the span in both directions is 2825 mm, and the length of the shear link is 350 mm. The section of the members is shown in Table 8.

Table 8 Cross sectional dimensions of the member

Member	Cross sectional dimensions (mm)	
Column	H145×145×8×10	
Beam	H140×100×8×10	
Brace	H100×100×6×10	
Shear link	1 st floor	H125×70×4×8
	2 nd floor	H100×70×4×8
	3 rd floor	H80×70×3×8

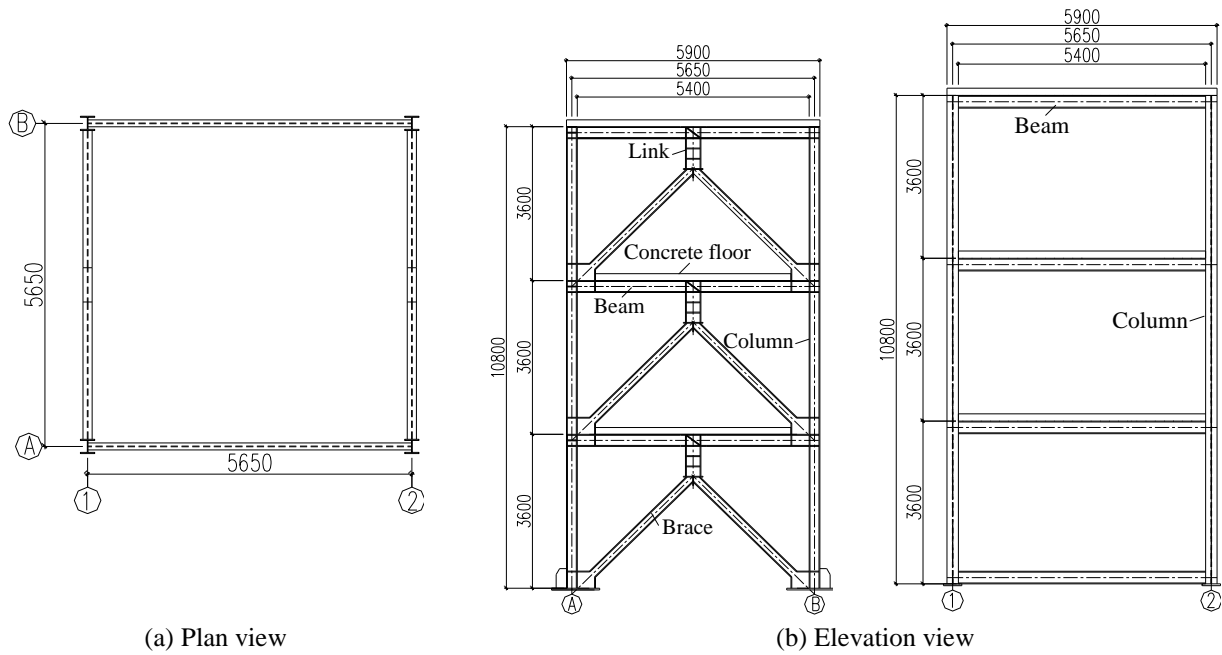


Fig. 7 The prototype structure

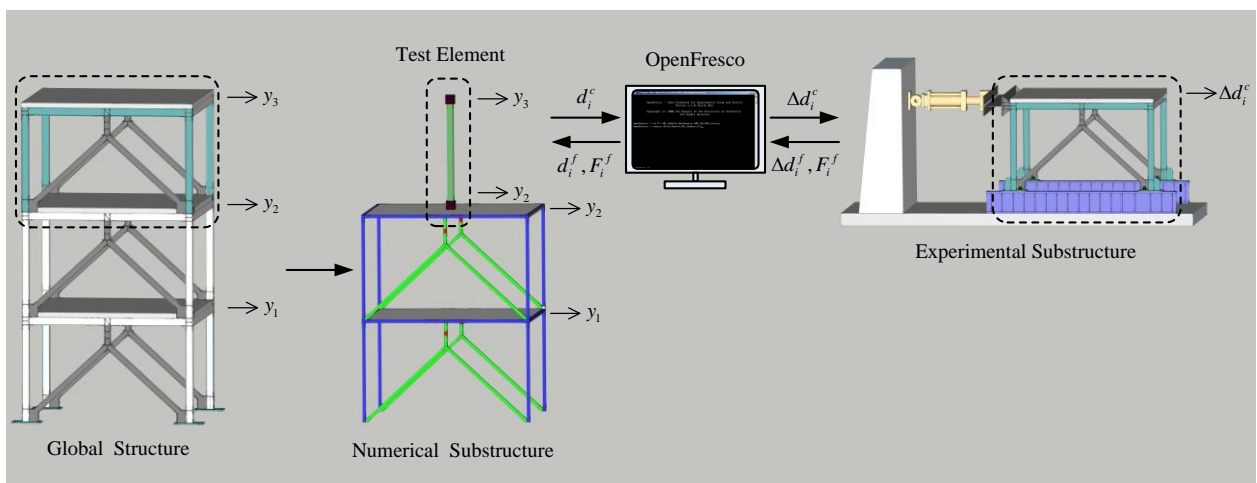


Fig. 8 SHST model

Before performing substructure division, it is necessary to understand the mechanical properties of each part of the global structural model to determine which part will be used as the experimental substructure. The nonlinear hysteretic behavior of EBFs during seismic events is complex and difficult to predict at large drift levels. If only the eccentrically braced part of the substructure is selected for testing, its boundary conditions will be complex and difficult to simulate. To better guarantee the boundary force conditions of eccentric braces, considering the spatial global effect of the frame structure, a SHST is conducted using the one-story frame model as the experimental substructure. In addition, the deformation compatibility between the frame beam-column with high strength steel and the link with common steel during an earthquake can also be observed and analyzed.

As shown in Fig. 8, for the model of the three-story prototype structure, a preliminary design analysis shows that compared with the first and second stories under seismic load, the top-story frame has the tendency to enter the plasticity zone first. Thus, when selecting the substructure, we take the top-story frame as the experimental substructure. The remaining two stories are used as the numerical substructure to carry out three-dimensional numerical modeling in OpenSees. The communication between the two substructures is carried out by the test beam-column element (Schellenberg *et al.* 2009) established in the OpenFresco test platform. The test element is an important module in OpenFresco. It can be used to represent the experimental substructure in the OpenFresco software system. In this paper, OpenSees Navigator (OSN) (Tony and Andreas 2009), a pre-and post-



Fig. 9 Test setup of experimental substructure

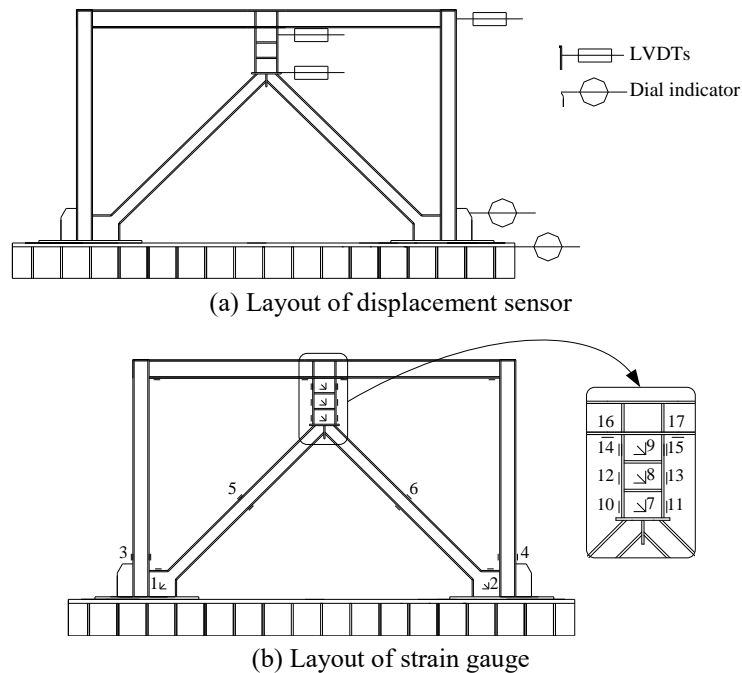


Fig. 10 Instrumentation arrangement of experimental substructure

Table 9 Material properties of steel

Steel	Thickness (mm)	Yield strength f_y (MPa)	Ultimate strength f_u (MPa)	Elastic modulus E (10^5 MPa)	Elongation δ (%)
Q235	3.01	283.1	397.1	2.14	31.57
Q235	4.05	271.9	402.1	2.17	31.83
Q235	8.11	276.7	421.1	2.18	32.18
Q345	6.04	414.2	542.08	2.11	28.36
Q345	10.11	362.8	545.60	2.01	28.84
Q460	8.06	475.1	634.42	2.12	25.38
Q460	9.97	515.9	691.46	2.06	23.65

processing software for OpenSees, is used to model. OpenFresco's test setup module embedded in OSN, so the whole modeling process no longer needs to be realized using a Tool Command Language, which greatly reduces the test threshold and helps to promote the SHST.

3.2.1 Experimental substructure

The experimental substructure occupies the third story

of the global structure. The material properties of steel obtained by coupon test are shown in Table 9. The test setup is shown as the experimental substructure in Fig. 9. The column foot and the ground beam are connected by the anchor bolts. A 100-t MTS hydraulic servo actuator was used for loading as a single particle in SHST. One end of the actuator is fixed on the reaction wall and the other end is connected with the middle point of the distribution beam

Table 10 Definition parameter of shear material

Shear hinge	Steel02	1 st floor value	2 nd floor value	3 rd floor value
Shear force V_y (Eq. (1))	Yield strength f_y	78.667 kN	61.382 kN	37.373 kN
Line stiffness K_0 (Eq. (3))	Elastic modulus E	104.209 kN/mm	80.308 kN/mm	45.574 kN/mm
Strain hardening rate	b	0.01	0.01	0.01

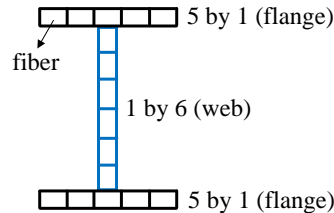


Fig. 11 Fiber section division

located at the height of the story. The whole loading process is displacement-controlled (with an accuracy of 0.001 mm), and the loading step is set to 0.5 s.

The measurement scheme of the experimental substructure is shown in Fig. 10, which mainly includes displacement and strain measurements. The lateral displacement value of the experimental substructure and the rotation value of the shear link are measured by the LVDTs, and the displacement of the column foot and the slip of the ground beam are measured by a dial indicator. The strain of the experimental substructure is measured by resistance strain gauges. The strain gauges are arranged at the flange of the beam-column joint, brace and shear link section, and the strain rosette is arranged at the web of the beam-column joint and shear link section. The strain measurement points near the shear link only indicate the strain numbers used in the subsequent analysis. Considering that the force on the shear link section is the largest in the Y-shaped eccentric brace, mainly the strain is analyzed herein.

3.2.2 Numerical substructure

The numerical substructure of the SHST model in this section is established based on the modeling study of Y-HSS-EBFs in Section 2. The concrete floor is assumed to be rigid. Force Beam-Column Elements, that can take into account the material nonlinearity, are used for the frame beams and columns. Truss Elements are used for braces. A fiber section is selected as the section type. Using the fiber section, the Force Beam-Column Elements can be divided along the cross-section into several fine fibers that can take the coupling relationship between the axial force and the bending moment of the components into account. As shown in Fig. 11, during the actual fiber section division process, the member is first divided into three parts by the flange and web, and then each part is subdivided into smaller fibers. According to the research of Du *et al.* (2012) on the sensitivity of fiber section division, the two flanges in the fiber section are divided into 5 by 1 fibers and the web is divided into 1 by 6 fibers. Steel02 is selected for the material, and concrete parameters are taken according to

material coupon test results as shown in Table 9. For the simulation of the shear link, shear hinges are located in the middle of the shear link using the method of zero-length elements combined with elastic elements. All shear deformation is concentrated in the hinges. The shear effect is simulated by the Steel02 material. The specific settings are shown in Table 10.

3.2.3 Communication between substructures

There are two key problems in SHST modeling: (1) how to realize the equivalence between the test element and experimental substructure; and (2) how to transform the boundary condition between the experimental and numerical substructures.

For problem 1, as the structure mass is mainly concentrated on the floor, the smaller beam-column mass can be equivalent to the floor position of the model. Meanwhile, considering that under the action of one-way horizontal earthquakes, the model with few stories produces the deformation mainly based on horizontal displacement, and the floor is absolutely rigid in its own plane, so only the horizontal displacement of the floor is considered as the dynamic degree of freedom. Then, a Beam-Column Test Element corresponding to the experimental substructure is established in the OSN. The bottom node of the test element is located in the center of the second floor slab, and the top node is located at the third floor. *Single-Point Constraints* are added to test element nodes to restrict their vertical and rotation displacements. The mass of the SHST model is concentrated at the node position of the story height, and the mass matrix is expressed as Eq. (4). The initial stiffness matrix K^e (Eq. (5)) of the experimental substructure is obtained by small displacement static loading, which is input into the definition of the test element as initial parameters

$$M = \begin{bmatrix} 0.00767 & 0.00767 & 0 & 0 & 0 & 0 \\ 0.00767 & 0.00767 & 0 & 0 & 0 & 0 \\ 0.00658 & 0.00658 & 0 & 0 & 0 & 0 \end{bmatrix} \text{kt} \quad (4)$$

Table 11 Sequence of the SHST

Serial number	Earthquake level	PGA/g	Serial number	Earthquake level	PGA (g)
1	Stiffness test	-	21	Stiffness test	-
2–4	Frequent 7	0.042	22–24	Seldom 7	0.264
5	Stiffness test	-	25	Stiffness test	-
6–8	Frequent 8	0.084	26–28	Seldom 8	0.480
9	Stiffness test	-	29	Stiffness test	-
10–12	Basic 7	0.120	30–32	Seldom 9	0.744
13	Stiffness test	-	33	Stiffness test	-
14–16	Frequent 9	0.168	34–36	-	1.0
17	Stiffness test	-	37	Stiffness test	-
18–20	Basic 8	0.240			

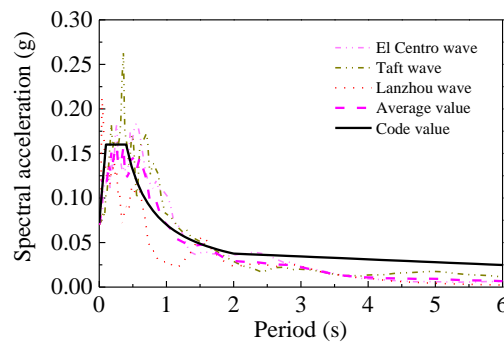


Fig. 12 Acceleration response spectra

$$K^c = [k_{11}] = [31.2] \text{ kN/mm} \quad (5)$$

For problem 2, it has been explained in problem 1 that only the horizontal displacement response of the experimental substructure is considered. First, the Multi-Point Constraint command in OpenSees: *Equal DOF* is used to ensure that the horizontal displacement response of the experimental substructure and the numerical substructure at the boundary is consistent in the SHST model by setting a master-slave relationship. Meanwhile, the absolute displacement d_i^c relative to the foundation is calculated by SHST model, whereas the actual experimental substructure is fixed on the ground when loading, and the displacement applied by the actuator should be the inter-story drift Δd_i^c of the third story of the model.

In order to achieve the above command conversion, as shown in Fig. 8, it is assumed that during an earthquake, the displacement response of each story of the prototype structure is y_1 , y_2 , and y_3 respectively. In the corresponding SHST model, the displacement response of the first and second stories of the numerical substructure is y_1 and y_2 respectively, the displacement response at the bottom of the test element is y_2 , and the displacement response at the top of the test element is y_3 . Then, the experimental control module in OpenFresco is used to convert the command displacement $d_i^c = y_3$ calculated by

the test element into relative displacement $\Delta d_i^c = y_3 - y_2$ and send it to the actuator. The actuator imposes this step command to obtain feedback displacement Δd_i^f and feedback force F_i^f . Finally, Δd_i^f and F_i^f are sent back to the test element through OpenFresco for further analysis of the SHST model.

3.2.4 Loading protocol

GB5011-2010 stipulates that the acceleration time history curve of actual strong earthquake record and artificial simulation shall be selected according to the type of construction site and the grouping of design earthquake, in which the number of actual strong earthquake record shall not be less than two-thirds of the total number. The average seismic influence coefficient curve of multiple time history curves is consistent with that of the mode decomposition response spectrum method in a statistical sense. According to GB5011-2010, two actual strong earthquake records (El Centro wave, Taft wave) and one artificial simulation wave (Lanzhou wave) are selected as the inputs for the original seismic wave. The acceleration response spectrum and average values of the three seismic waves are compared with the standard spectrum, as shown in Fig. 12. The seismic waves of each level are in the order of El Centro, Taft and Lanzhou waves. The specific load protocol is shown in Table 11. The acceleration similarity ratio is 1.2:1. The stiffness of the substructure is obtained

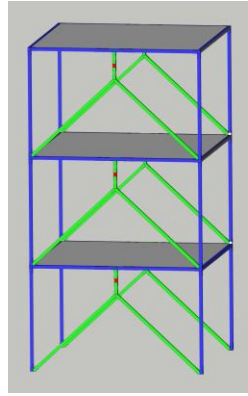


Fig. 13 Numerical model of global structure



(a) Peeling of welding seam



(b) Rust peel off



(c) Residual deformation of shear link



(d) Crack in welding seam at link to brace connection



(e) Welding seam breakage at link flange to beam connection



(f) Partial fracture at link web to beam connection



(g) Completely torn at link to beam connection



(h) Full fracture of welding seam at link flange to brace connection

Fig. 14 SHST phenomena

by small displacement loading at the beginning of the test and after the end of each loading stage. Rayleigh damping is used for structural damping, 0.045 for frequent earthquakes and 0.05 for seldom earthquakes.

3.2.5 Global numerical model of the structure

A numerical model of the global structure is established, which is mainly used to compare the results of the follow-up SHST. As shown in Fig. 13, the modeling of columns,

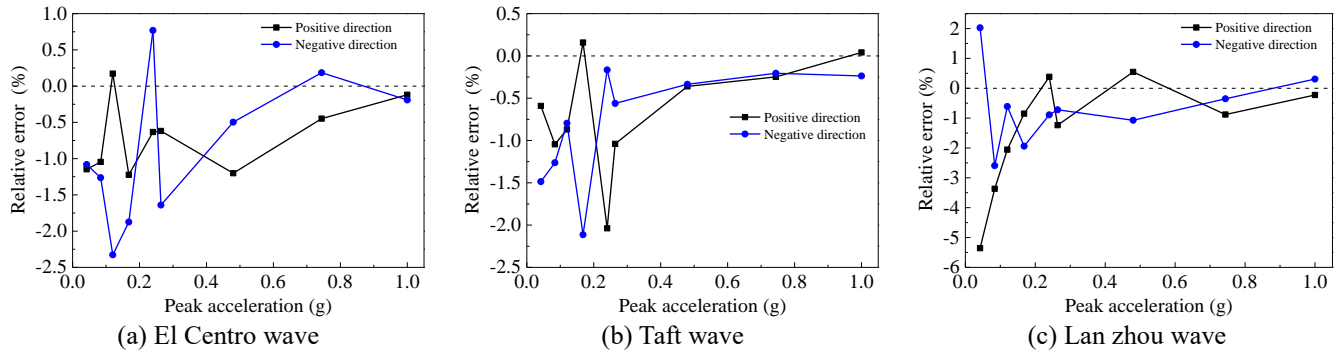


Fig. 15 Relative error of peak displacement

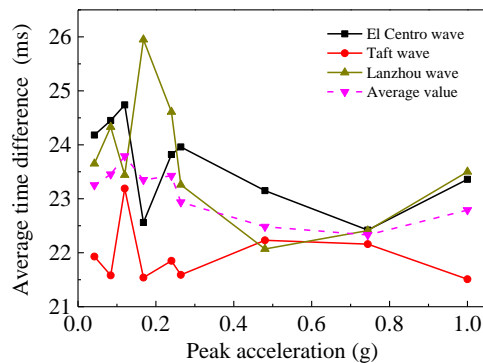


Fig. 16 Difference of loading time

beams, braces and shear links of two stories below are consistent with the numerical substructure. The shear material parameters of the third story shear link are shown in Table 10.

3.2.6 SHST phenomenon

During the entire test process, the deformation of the experimental substructure mainly occurs at the shear link section. Under a seldom 7 intensity loading stage (0.264 g), the weld peeling (see Fig. 14(a)) and rust peeling (see Fig. 14(b)) appeared at the connection between the web and flange of the shear link section. After the El Centro wave with a peak acceleration of 0.480 g, the rust skin shedding became more obvious, and a certain extent residual deformation of the shear link appeared (see Fig. 14(c)). Under the action of the El Centro wave with a seldom 9 intensity (0.744 g), cracks in welding seams appeared at the connection between the shear link and the brace at the south side of the model (see Fig. 14(d)), and welding seam breakage appeared at the shear link flange to the frame beam at the north side (see Fig. 14(e)). After the peak ground acceleration reached 1.0 g, there was a partial fracture at the link web to beam connection on the south side of the specimen (see Fig. 14(f)). The link to beam connection on the north side was completely torn (see Fig. 14(g)), and the flange weld on the brace joint underwent almost full fracture (see Fig. 14(h)).

4. Validation of the SHST model

4.1 Stability analysis of the test platform

Fig. 15 shows the relative error between the feedback displacement of the actuator and the command displacement of the test element under each loading stage. It can be seen that the peak value of the feedback displacement is close to the peak value of the command displacement in most cases, and the maximum error occurs in the negative direction (pull) under the action of the Lanzhou wave with frequency 7 intensity (0.042 g), which is 5.357%. When the PGA of the seismic wave is small, the slight displacement response places higher requirements on the loading performance of the actuator, resulting in larger relative error. With the peak value of the displacement response increases, the relative error first decreases, and then gradually stabilizes, which met the loading error limit set by the actuator.

Fig. 16 shows the each step average time difference between the actual actuator loading and the planned loading under different loading stages. It can be seen that the change of peak acceleration of the seismic wave has little effect on the loading time difference. All the differences are in the range of 21–26 ms. The average value for all loading stages is approximately 23 ms, which mainly includes finite element simulation analysis, OpenFresco data communication, and the approximate loading and stabilization process of the actuator. In the non-real-time SHST, its influence can be neglected.

Table 12 Comparison of performance indicators

Seismic excitation	PGA (g)	First floor			Second floor			Third floor		
		SHST (mm)	Global numerical model (mm)	Relative error (%)	SHST (mm)	Global numerical model (mm)	Relative error (%)	SHST (mm)	Global numerical model (mm)	Relative error (%)
El Centro wave	0.480	4.295	3.967	8.268	7.942	7.038	12.831	12.651	11.289	12.066
	0.744	5.623	6.327	-11.140	11.447	12.600	-9.151	20.780	18.086	14.895
Taft wave	0.480	4.455	4.246	4.922	8.904	8.982	-0.868	14.982	13.338	12.328
	0.744	5.687	6.508	-12.623	11.754	13.03	-9.792	22.188	19.259	15.209
Lanzhou wave	0.480	3.159	2.887	9.421	6.896	6.321	9.089	10.704	9.675	10.627
	0.744	3.780	3.301	14.526	8.321	7.143	16.486	15.100	12.987	16.272

Table 13 Maximum roof drifts of SHST model

PGA (g)	0.042	0.084	0.120	0.168	0.240	0.264	0.480	0.744	1.0
El Centro wave	1/2918	1/1827	1/1319	1/1144	1/737	1/705	1/426	1/259	1/199
Taft wave	1/2727	1/1415	1/989	1/927	1/749	1/645	1/360	1/243	1/173
Lanzhou wave	1/4923	1/3576	1/2396	1/1721	1/1215	1/1187	1/504	1/357	1/262

Table 14 Maximum inter-story drifts of SHST model

PGA (g)	0.042	0.084	0.120	0.168	0.240	0.264	0.480	0.744	1.0
1st floor	1/2278	1/1193	1/834	1/781	1/629	1/595	1/404	1/296	1/255
2nd floor	1/2913	1/1895	1/1295	1/1041	1/775	1/634	1/404	1/316	1/258
3rd floor	1/2307	1/1282	1/896	1/842	1/652	1/630	1/296	1/172	1/105

4.2 SHST model validation

The test analysis results of the SHST model under different loading stages are verified by comparing the displacement responses of the floors of the SHST model and the global numerical model under seldom 8 and seldom 9 leveling conditions. Among them, the displacement values of the first and second stories of the SHST model are obtained by numerical substructure analysis, and the displacement values of the third story are obtained by the displacement sensor of the experimental substructure plus the displacement values of the second story. The global numerical model is directly obtained using OpenSees simulation. From Table 12, it can be seen that the experimental results of the SHST model under seismic load are basically consistent with those of the global numerical model of the whole structure based on OpenSees. The errors of individual loading stages under seldom 9 intensity conditions exceed 15%. This is mainly due to the obvious non-linear seismic response of the structure under seldom earthquakes, and the weld fracture occurs in the shear link of the experimental substructure, which results in the deviation between the overall analysis results of the SHST model and the simulation results of the global numerical model.

5. Test results of seismic performance

5.1 Overall displacement response

According to the measured displacement of the experimental substructure and the analysis of the displacements of the numerical substructure, the overall maximum roof drifts of the SHST model under different loading stages are calculated. As shown in Table 13, it can be seen that the response of the model under the Lanzhou wave is the smallest, while the results for the El Centro and Taft waves are relatively close. Under the action of frequent earthquakes, the maximum roof drifts do not differ significantly, which indicates that the overall displacement response of the structure is small. After seldom 8 intensity loading stages, the maximum roof drifts of the whole model changed significantly.

Table 14 shows the maximum inter-story drifts of the SHST model under different loading stages. It can be seen that the maximum inter-story drift of the model structure is 1/784 under the action of frequent earthquakes, which meets the requirement of the current standard GB 50011-2010 that the elastic inter-story drift of multi-story and high-rise steel structures is less than 1/250. The maximum inter-story drift of the model structure under seldom earthquakes is 1/105, which is less than the 1/50 limit value for elastic-plastic inter-story drift of multi-story and high-rise steel structures in GB 50011-2010. It shows that the

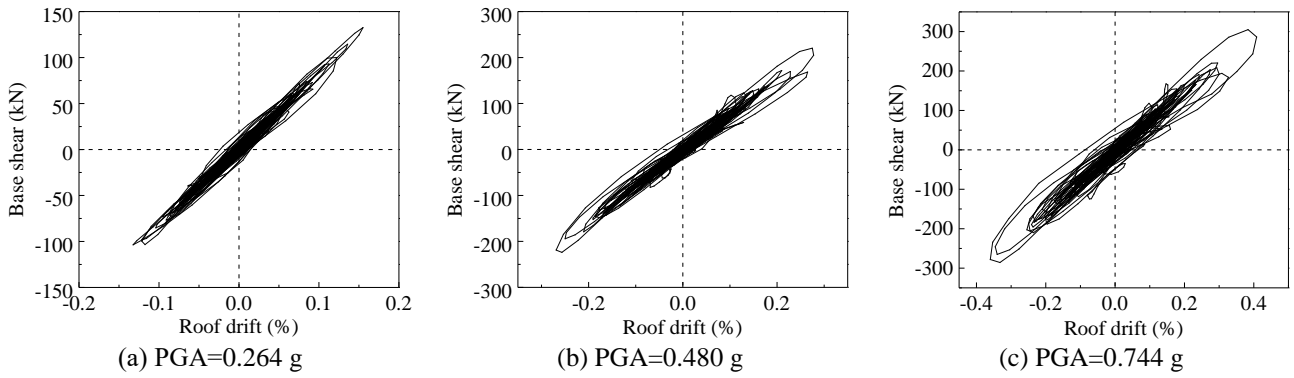


Fig. 17 Hysteretic curves of base shear and roof drift

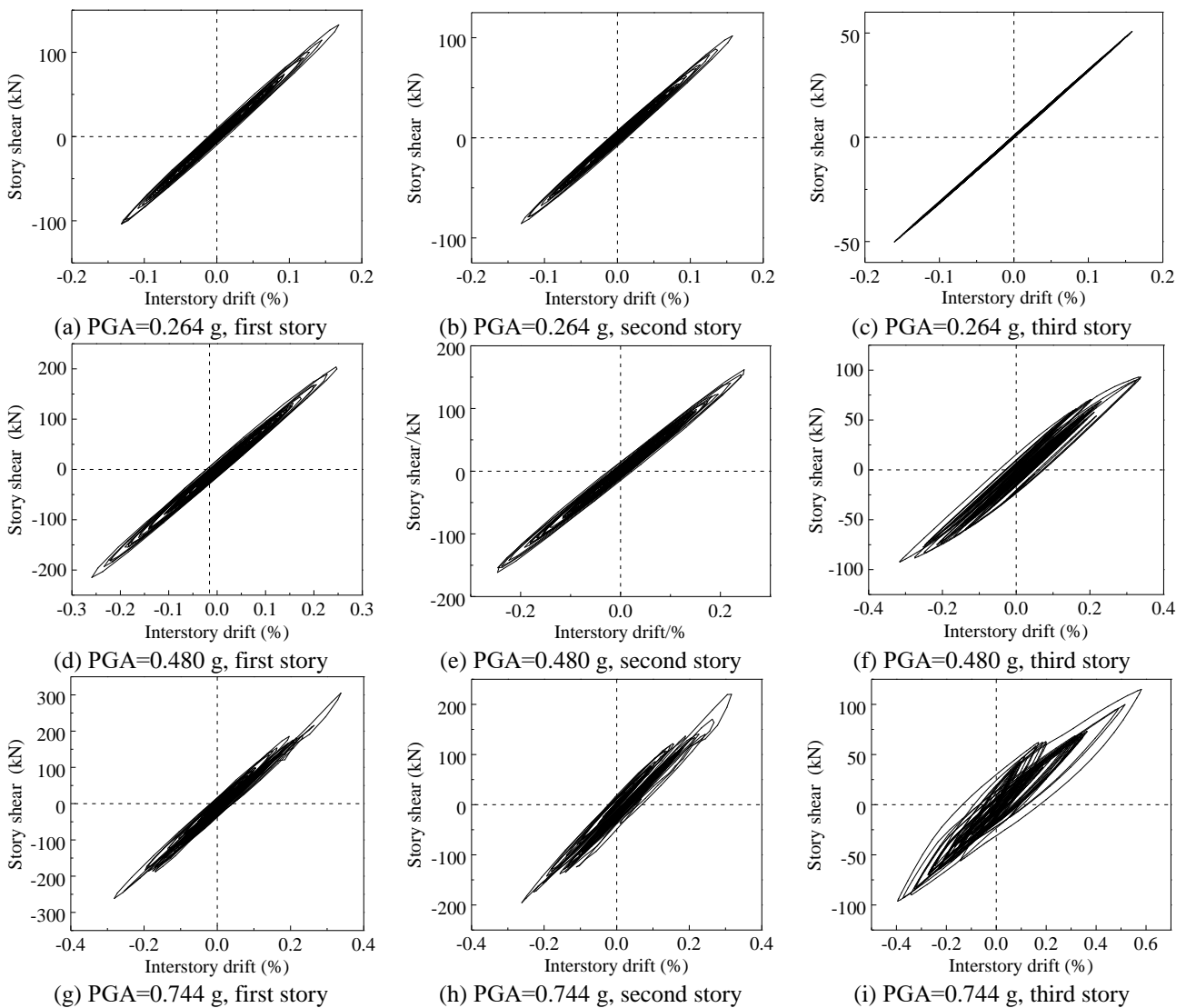


Fig. 18 Hysteretic curves of story shear and inter-story drift

structure can still meet the requirements of deformation limitation of the code even though local damage occurs in the case of seldom earthquakes.

5.2 Hysteretic behavior

Fig. 17 shows the base shear-roof drift hysteresis curves of the model under different intensity Taft waves, in which the base shear is obtained from the sum of the numerical

Table 15 Key points of skeleton curves and ductility factor

Position	Loading direction	Yield point		Ultimate point		Ductility $\mu = \theta_u / \theta_y$
		Drift θ_y (%)	Shear F_y (kN)	Drift θ_u (%)	Shear F_u (kN)	
First story	Positive	0.308	269.052	0.422	314.172	1.370
	Negative	-0.276	-248.364	-0.381	-290.141	1.380
Second story	Positive	0.282	198.264	0.407	244.712	1.443
	Negative	-0.253	-182.219	-0.371	-224.214	1.466
Third story	Positive	0.297	82.745	0.952	135.729	3.205
	Negative	-0.276	-81.806	-0.752	-115.211	2.724

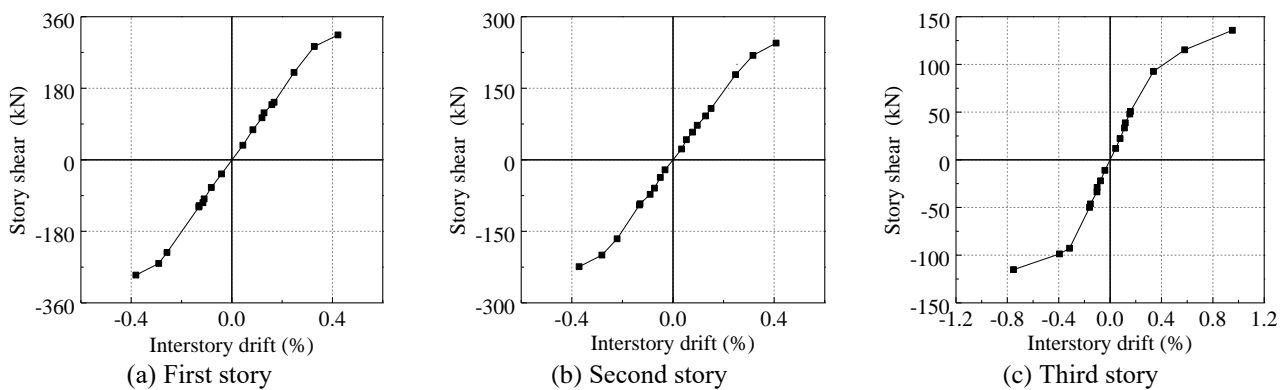


Fig. 19 Skeleton curves

substructure simulation results and the feedback force of the experimental substructure actuator. It can be seen from the graph that the model is basically in an elastic state under the action of seldom 7 intensity earthquakes. Under seldom 8 intensity earthquakes, the residual deformation of the model appears, and the non-linear characteristics are more obvious. After seldom 9 intensity earthquakes, the weld seam between the flange of the shear link and that of the frame beam fractures, and the model enters into plasticity, forming a clear hysteretic loop.

Fig. 18 shows the story shear-inter story drift hysteresis curve of the model under different strengths of the Taft wave. It can be seen that the structure of each story is in the elastic stage under the seldom 7 intensity loading stage, and the hysteretic curve is basically a straight line. The first and second stories of the model are still in the elastic stage under the seldom 8 intensity loading stage, and the third story of the structure has the tendency of entering the plastic domain. After the seldom 9 intensity loading stage, the first and second stories of the model have a tendency of forming hysteretic loops. Due to partial cracking of the shear link section, hysteresis loops occur when the structure enters the plastic domain, and the obvious trend of stiffness reduction can be seen.

5.3 Skeleton curves

A skeleton curve is the envelope of the hysteretic curve obtained under different intensity PGAs. It can reflect the yield load, ultimate load, and ductility of each story of the

test model under seismic loading. The skeleton curves of the SHST model under different intensities of the Taft wave are shown in Fig. 19. Before a seldom 8 intensity loading stage, each story of the SHST model is in the elastic stage, and the displacement response of each story is similar. There is a linear relationship between the inter-story drift and the story shear. After the seldom 8 intensity loading stage, compared with that of the first and second stories, the stiffness of the third story of the SHST model decreases more evidently, and the inter-story drift reaches 0.337%. In the SHST model, the numerical substructure will return to the initial elastic state after each loading condition whereas damage accumulation will occur in the experimental substructure. Thus, when the SHST model enters the elastic-plastic loading stage, the displacement response of the third story will change more with an increase in earthquake intensity compared with the other two stories. This phenomenon is also consistent with the displacement response comparison of the SHST model and the global numerical model in Section 4.2.

Table 15 summarizes the key point parameters of the skeleton curves and the ductility factors of each story. As there is no obvious descending section in the skeleton curve, the ultimate point is the peak point of the maximum loading stage. All the stories of the SHST model exhibit similar yielding displacements. The ductility factor is the ratio of the ultimate inter-story drift to the yield inter-story drift. It can be observed that the ductility factor of the third story of the SHST model reaches 3.205, which indicates that the experimental substructure exhibits good ductility in the elastic-plastic stage.

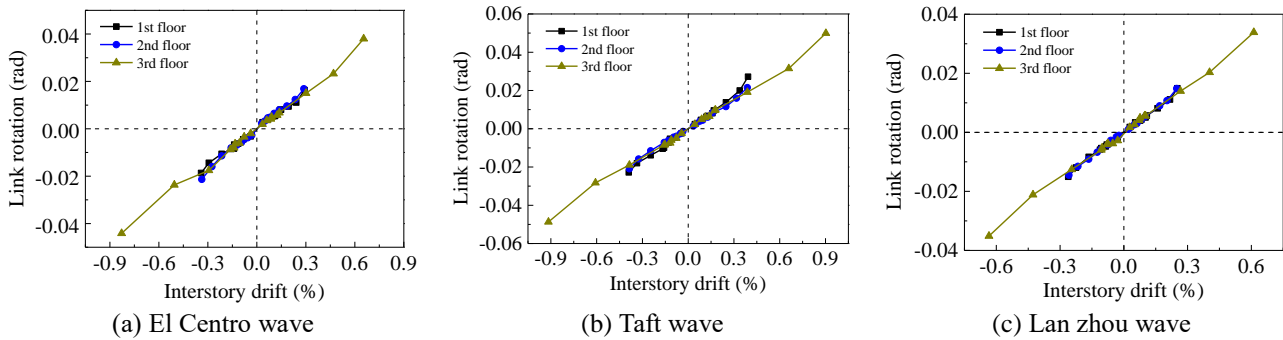


Fig. 20 Graph of inter story versus link rotation

5.4 Rotation of the shear link

Fig. 20 shows the relationship between the maximum shear link rotation of each story and the maximum inter story drift at the corresponding stories under different loading stages. It can be seen from the graph that before seldom 8 intensity loading stages, the maximum shear link rotation and inter story drift basically change linearly in a positive proportion, indicating that the model is in an elastic state. After the seldom 8 intensity loading stage, the stiffness of the whole model degrades due to the plasticity of the shear link. Especially when the peak acceleration reaches 1.0 g, the slope of the broken line increases obviously. From Table 14, it can be seen that the inter-story drift of the third story of the model is the largest, so the rotation of the shear link of the corresponding story is also the largest. Considering the cumulative damage of the third-story experimental substructure of the SHST model in the test process, the shear link rotation changes remarkably after the seldom 8 intensity condition. The maximum rotation of the shear link is 0.0498 rad after the Taft wave with an acceleration of 1.0 g, which is less than the limit value of the shear yield link of AISC341-16 (2016) with $\gamma_p \leq 0.08$ rad.

5.5 Stiffness degradation of the experimental substructure

During the SHST, the lateral stiffness of the experimental substructure was measured by the actuator under each stage of the loading condition. As shown in Fig. 21, it can be seen that the stiffness of the model undergoes little change compared with the initial stiffness under frequent earthquakes, indicating that the structure is still in an elastic state, which is basically consistent with the experimental phenomena. When the peak value of input acceleration reaches 0.480 g, the weld cracks slightly and the stiffness of the model decreases significantly. When the peak acceleration reaches 1.0 g, the stiffness degradation rate of the model reaches 49.1%. At this time, the shear link fails almost completely, basically only the high-strength steel frame is subjected to seismic force, which also conforms to the idea of multi-aspect seismic fortification.

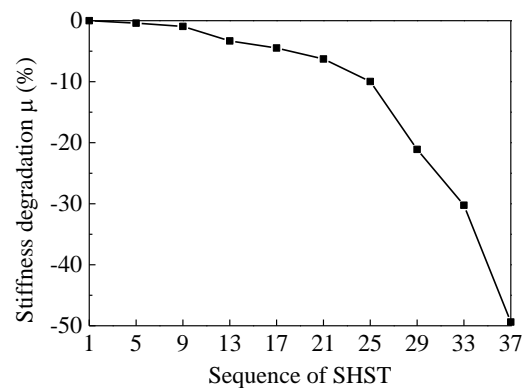


Fig. 21 Stiffness degradation of experimental substructure

5.6 Strain analysis of the experimental substructure

Fig. 22 shows the measured strain responses of the experimental substructure under the El Centro, Taft, and Lanzhou waves. The corresponding strain $\varepsilon/\varepsilon_y$ in the figure is the ratio of measured strain to yield strain. It can be seen that the strain value at the web of the shear link (M 7–M 9) is obviously higher than that at the flange (M 10–M 15), which indicates that the shear link section is dominated by shear deformation, and the strain value at the web of the shear link (M 7–M 9) is always greater than that at the corresponding beam-column joints (M 1–M 4), which conforms to the design idea of this structure. The strain value of each measuring point increases steadily and the difference is small between the frequent 7 and seldom 7 intensity loading stages, and the structure is in an elastic state at this time ($\varepsilon/\varepsilon_y < 1$). After the seldom 8 intensity loading stage, the strain values of the web of the shear link (M 7–M 9) exceed the yield strain ($\varepsilon/\varepsilon_y > 1$), which indicates that the structure has entered the plastic stage and started to dissipate seismic energy. When the peak acceleration reaches 1.0 g, the strain value of the measuring point 7–9 at the web of the shear link has increased significantly. At the same time, it can be seen that the flange measuring points 14 and 15 of the shear link here have also entered yield due to the maximum force at the link to frame beam connection. In the Y-HSS-EBF system in this study, high-strength steel (Q460) is used in the frame beam and

column, and ordinary steel (Q235) is used in the shear link. Therefore, under the action of seismic load, the shear link first undergoes plastic deformation and dissipates energy, while the frame beam and column can still maintain elasticity, thus realizing the purpose of multi-aspect seismic fortification.

6. Conclusions

The SHST is an efficient method of performing large-scale seismic testing of complex structures. In this study, the SHST was performed on a half-scale three-story on e-by-one bay Y-HSS-EBF model. The following conclusions can be drawn from this research:

- The pseudo-static hysteretic analysis of the existing test has been successfully simulated by using OpenSees. The comparison between the finite element results and the test results verifies the validation of the numerical model, which indicates that OpenSees can be used to establish the numerical substructure model of a Y-HSS-EBF.

- The method of using the test beam-column element in OpenFresco to model the experimental substructure of space frame has been proved to be reasonable. The peak value of feedback displacement of the actuator is close to the peak value of the command displacement of test element. The analysis results of the hybrid simulation model are in good agreement with those of the numerical model of the global structure. It was shown that the SHST based on OpenFresco has good stability and accuracy.

- The maximum inter-story drifts of the SHST model under frequent and seldom earthquakes are 1/781 and 1/105, respectively, which conform to the limits of the seismic design code. Before seldom 8 intensity loading stages, the story shear, maximum shear link rotation and inter-story drift change linearly in proportion. After the seldom 8 intensity loading stage, the stiffness of the entire model degrades due to the plasticity of the shear link. The maximum rotation of the shear link is 0.0498 rad after the Taft wave with an acceleration of 1.0 g, which is less than the limit value of the shear yield link of AISC341-16 with $\gamma_p \leq 0.08\text{rad}$.

- The strain analysis of the experimental substructure shows that the shear link section is dominated by shear deformation. After the seldom 8 intensity loading stage, the strain values of the web of the shear link exceed the yield strain, which indicates that the structure has entered the plastic stage and started to dissipate seismic energy, while the frame beam and column still maintain elasticity, thus realizing the purpose of multi-aspect seismic fortification. When the peak acceleration reaches 1.0 g, the stiffness degradation rate of the experimental substructure reaches 49.1%. At this time, the shear link almost completely fails, basically only the high-strength steel frame is subjected to seismic force.

Acknowledgments

The authors are grateful for the financial support from the National Natural Science Foundation of China (Grant No. 51178382).

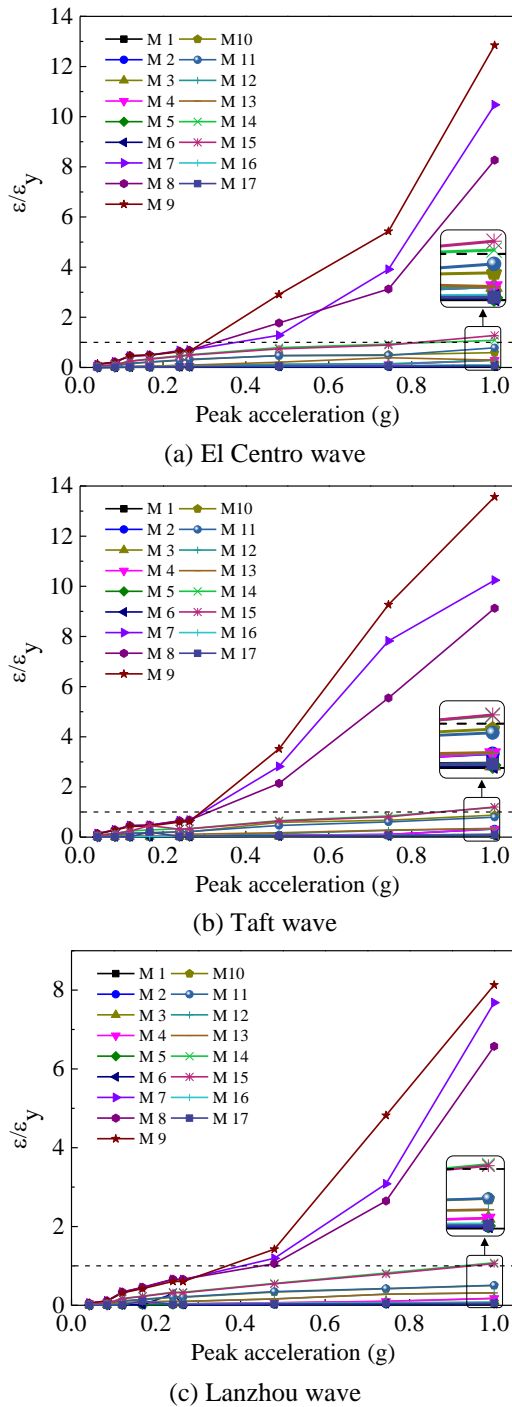


Fig. 22 Variation of strain of experimental substructure

References

- AISC341-16 (2016), Seismic Provision for Structure Steel Buildings, American Institute of Steel Construction; Chicago, USA.
- Alhendi, H. and Celikag, M. (2015), "Behavior of reverse-channel and double-reverse-channel connections to tubular columns with HSS", *J. Constr. Steel Res.*, **112**, 271-281. <https://doi.org/10.1016/j.jcsr.2015.05.017>.
- Ban, H.Y. and Shi, G. (2017), "A review of research on high-strength steel structures", *Proceedings of the Institution of Civil Engineers-Structures and Buildings*, **171**(8), 625-641.
- Chae, Y., Ricles, J.M. and Sause, R. (2013), "Large-scale experimental studies of structural control algorithms for structures with magneto-rheological dampers using real-time hybrid simulation", *J. Struct. Eng.*, **139**, 1215-1226. [https://doi.org/10.1061/\(ASCE\)ST.1943-541X.0000691](https://doi.org/10.1061/(ASCE)ST.1943-541X.0000691).
- Chiew, S.P., Zhao, M.S. and Lee, C.K. (2015), "Fatigue performance of high strength steel built-up box T-joints", *J. Constr. Steel Res.*, **106**, 296-310. <https://doi.org/10.1016/j.jcsr.2014.12.018>.
- Dermitzakis, S.N. and Mahin, S.A. (1985), "Development of substructuring techniques for on-line computer controlled seismic performance testing", Research Report No.UCB/EERC-85/04; Berkeley, CA, Earthquake Engineering Research Center.
- Du, K., Sun, J.J. and Xu, W.X. (2012), "The division of element, section and fiber in fiber model", *J. Earthq. Eng. Eng. Vib.*, **32**(5), 39-46.
- Duan, L.S. and Su, M.Z. (2017), "Seismic testing of high-strength steel eccentrically braced frames with a vertical link", *Proceedings of the Institution of Civil Engineers-Structures and Buildings*, **170**(11), 874-882.
- GB 50011-2010 (2016 edition) (2016), Code for Seismic Design of Buildings, China Architecture and Building Press; Beijing, China.
- Hashemi, M.J. and Mosqueda, G. (2014), "Innovative substructuring technique for hybrid simulation of multistory buildings through collapse", *Earthq. Eng. Struct. D.*, **43**(14), 2059-2074. <https://doi.org/10.1002/eqe.2427>.
- Kasai, K. and Popov, E.P. (1986), "General behavior of WF steel shear link beams", *J. Struct. Eng.*, **112**(2), 362-382. [https://doi.org/10.1061/\(ASCE\)0733-9445\(1986\)112:2\(362\)](https://doi.org/10.1061/(ASCE)0733-9445(1986)112:2(362)).
- Khan, M.A., Jiang, L., Cashell, K.A. and Usmani, A. (2018), "Analysis of restrained composite beams exposed to fire using a hybrid simulation approach", *Eng. Struct.*, **172**, 956-966. <https://doi.org/10.1016/j.engstruct.2018.06.048>.
- Kim, D.K., Lee, C.H., Han, K.H., Kim, J.H., Lee, S.E. and Sim, H.B. (2014), "Strength and residual stress evaluation of stub columns fabricated from 800 MPa high-strength steel", *J. Constr. Steel Res.*, **102**, 111-120. <https://doi.org/10.1016/j.jcsr.2014.07.007>.
- Lian, M., Su, M.Z. and Guo, Y. (2015), "Seismic performance of eccentrically braced frames with high strength steel combination", *Steel Compos. Struct.*, **18**(6), 1517-1539. <https://doi.org/10.12989/scs.2015.18.6.1517>.
- Mansour, N., Christopoulos, C. and Tremblay, R. (2011), "Experimental validation of replaceable shear links for eccentrically braced steel frames", *J. Struct. Eng.*, **137**(10), 1141-1152. [https://doi.org/10.1061/\(ASCE\)ST.1943-541X.0000350](https://doi.org/10.1061/(ASCE)ST.1943-541X.0000350).
- Mazzoni, S., McKenna, F., Scott, M.H. and Fenves, G.L. (2009), *Open system for earthquake engineering simulation user command-language manual—OpenSees version 2.0*, Pacific Earthquake Engineering Research Center (PEER), Univ. of California, Berkeley, CA, USA.
- Menegotto, M. and Pinto, E. (1973), "Method of analysis for cyclically loaded RC plane frames including changes in geometry and non-elastic behavior of elements under combined normal force and bending", *IABSE symposium on resistance and ultimate deformability of structures acted on by well defined repeated loads*, Lisbon, Portugal.
- Montuori, R., Nastro, E. and Piluso, V. (2014a), "Theory of plastic mechanism control for eccentrically braced frames with inverted y-scheme", *J. Constr. Steel Res.*, **92**(1), 122-135. <https://doi.org/10.1016/j.jcsr.2013.10.009>.
- Montuori, R., Nastro, E. and Piluso, V. (2014b), "Rigid-plastic analysis and moment-shear interaction for hierarchy criteria of inverted Y EB-Frames", *J. Constr. Steel Res.*, **95**(4), 71-80. <https://doi.org/10.1016/j.jcsr.2013.11.013>.
- Özhendekci, D. and Özhendekci, N. (2008), "Effects of the frame geometry on the weight and inelastic behaviour of eccentrically braced chevron steel frames", *J. Constr. Steel Res.*, **64**(3), 326-343. <https://doi.org/10.1016/j.jcsr.2007.07.009>.
- Popov, E.P. (1983), "Recent research on eccentrically braced frames", *Eng. Struct.*, **5**(1), 3-9. [https://doi.org/10.1016/0141-0296\(83\)90034-2](https://doi.org/10.1016/0141-0296(83)90034-2).
- Ricles, J.M. and Popov, E.P. (1994), "Inelastic link element for EBF seismic analysis", *Struct. Eng.*, **120**(2), 441-463. [https://doi.org/10.1061/\(ASCE\)0733-9445\(1994\)120:2\(441\)](https://doi.org/10.1061/(ASCE)0733-9445(1994)120:2(441)).
- Schellenberg, A., Kim, H.K., Takahashi, Y., Fenves, G.L. and Mahin, S.A. (2009), *OpenFresco Command Language Manual*, The Regents of the University of California, CA, USA, 35-37.
- Shayanfar, M.A., Barkhordari, M.A. and Rezaeian, A.R. (2012), "Experimental study of cyclic behavior of composite vertical shear link in eccentrically braced frames", *Steel Compos. Struct.*, **12**(1), 13-29. <https://doi.org/10.12989/scs.2012.12.1.013>.
- Shayanfar, M.A., Rezaeian, A.R. and Zanganeh, A. (2012), "Seismic performance of eccentrically braced frame with vertical link using PBPD method", *Struct. Des. Tall Spec.*, **23**(1), 1-21. <https://doi.org/10.1002/ta1.1015>.
- Shi, G., Liu, Z., Ban, H.Y., Zhang, Y., Shi, Y.J. and Wang, Y.Q. (2012), "Tests and finite element analysis on the local buckling of 420 MPa steel equal angle columns under axial compression", *Steel Compos. Struct.*, **12**(1), 31-51. <https://doi.org/10.12989/scs.2012.12.1.031>.
- Tony, Y. and Andreas, S. (2015), *OpenSees Navigator ver. 2.5.5*, Pacific Earthquake Engineering Research Center (PEER), Berkeley, CA, USA.
- Wang, F., Su, M.Z., Hong, M., Guo, Y.R. and Li, S.H. (2016), "Cyclic behaviour of Y-shaped eccentrically braced frames fabricated with high-strength steel composite", *J. Constr. Steel Res.*, **120**(2), 176-118. <https://doi.org/10.1016/j.jcsr.2016.01.007>.

BU